

Data-assisted physical modeling of oxygen precipitation in silicon wafers

Cite as: J. Appl. Phys. 125, 165705 (2019); doi: 10.1063/1.5090121

Submitted: 24 January 2019 · Accepted: 4 April 2019 ·

Published Online: 25 April 2019



Yi Yang,¹ Andreas Sattler,²  and Talid Sinno^{1,a)} 

AFFILIATIONS

¹Department of Chemical and Biomolecular Engineering, University of Pennsylvania, Philadelphia, Pennsylvania 19104, USA

²Siltronic AG, Hanns-Seidel-Platz 4, 81737 München, Germany

^{a)}Author to whom correspondence should be addressed: talid@seas.upenn.edu

ABSTRACT

A quantitative continuum model for oxide precipitation in silicon is presented that accounts for vacancy absorption and shape change as mechanisms of precipitate stress relief. All model parameters except one, the Si/SiO₂ interface free energy, are fixed at values established in prior studies of microdefect formation. The interface free energy is described by an 8-parameter function, whose functional form and dependencies were based on an analysis of electronic structure calculations of small oxide cluster thermodynamics. The interface energy function parameters are regressed, using global optimization, to an experimental benchmark consisting of 13 wafer thermal anneals, with different temperature-time histories and resulting in widely varying measured final oxide precipitate densities. We demonstrate that the model is able to capture the benchmark features well with multiple parameter combinations and that additional constraints are required to fully specify a unique solution. We also show that a simple, single-parameter, constant interface free energy model cannot fully capture the diverse experimental benchmark, highlighting the complexity of oxide precipitation. The precipitation model is used to analyze the mechanisms responsible for several features of oxide nucleation and growth during wafer annealing.

Published under license by AIP Publishing. <https://doi.org/10.1063/1.5090121>

I. INTRODUCTION

Oxide precipitation in Czochralski (CZ) silicon is one of the most important processes that impact the quality of wafers used for microelectronic device fabrication. Oxygen atoms, which are supplied by the silica crucible liners used to contain the Si melt, are incorporated into CZ crystals during growth and become supersaturated to varying degrees during crystal growth and subsequent wafer processing. Oxide precipitates are important microdefects because they provide gettering sites for detrimental metallic species introduced during wafer processing and also enhance the mechanical strength of large-diameter wafers.^{1–3} On the other hand, like other crystalline defects, such as voids and dislocation loops, they are undesirable in the surface region of the wafer where microelectronic devices are fabricated.⁴ Consequently, in a wafer with an ideal distribution of the oxide precipitates, the precipitate density away from the surface is high enough to ensure reliable intrinsic gettering, while near the surface of the wafer, a defect-free layer, or denuded zone (DZ), is present for device fabrication.²

Given the importance of oxygen precipitation, it is not surprising that modeling and quantitative prediction of oxygen precipitation

in wafer manufacturing has had a long history, and numerous analytical and computational models have been proposed.^{5–18} Yet, robust and comprehensive predictive capability remains elusive, in stark contrast with the modeling successes demonstrated in the case of void formation by vacancy aggregation.^{19–21} The primary reason for this relative lack of predictive ability is simply that oxide precipitation in silicon is surprisingly complex. This complexity is largely underpinned by the fact that oxide precipitation generates a large amount of internal compressive stress because the volume per silicon atom in the oxide phase (at any composition) is larger than that in the silicon matrix phase.²² The generated stress may be accommodated via several distinct mechanisms including (1) morphological changes of the precipitates, which may be observed in needle, plate or polyhedral shapes,¹⁷ (2) interaction with intrinsic point defects, namely, vacancy absorption and/or silicon interstitial emission,^{2,7} and possibly (3) changes in composition of the oxide.^{9,18}

In principle, the activation and relative importance of the various stress modulation pathways are strongly impacted by processing conditions both during bulk crystal growth and wafer thermal annealing treatments. However, the vast majority of oxide

precipitate engineering takes place in the setting of wafer thermal annealing because of the low thermal mass of wafers that allows rapid temperature changes and the proximity of surfaces that serve as sources and sinks for intrinsic point defects and oxygen atoms. Two broad wafer thermal annealing strategies have emerged for nucleating and growing oxide precipitates in sufficient quantities away from the device-active region. The so-called “Conventional Annealing” (CA) strategy employs long anneals at elevated temperature to create a lower oxygen concentration near the wafer surface by oxygen out-diffusion—the anneal length is determined by the slow oxygen diffusivity.^{13,23,24} Subsequent annealing at lower temperature drives oxide precipitate nucleation and growth everywhere in the wafer except in the depleted zone. A number of years ago, a much more efficient approach was introduced based on vacancy control of oxide precipitation.^{2,25} In this “Rapid Thermal Annealing” (RTA) approach, a short anneal followed by a rapid quench to lower temperature installs an inhomogeneous vacancy profile that exhibits vacancy supersaturation everywhere except in the near-surface region (due to equilibration at the surface). Subsequent annealing at a sequence of different temperatures leads to enhanced oxide precipitation facilitated by high vacancy availability everywhere except near the device-active surface.

The very different conditions and outcomes of oxide precipitation during CA and RTA have posed challenges for creating a unified, predictive model. Here, we attempt to produce such a model by including descriptions of the various stress relaxation mechanisms within a unified thermodynamic-kinetic picture. However, although many of the thermophysical properties, such as diffusivities and equilibrium concentrations, of intrinsic point defects are now well established,^{26–29} some of the key parameters describing oxide precipitates remain uncertain. Of these, the interface free energy between the oxide and Si matrix phase is both crucially important for model accuracy and very challenging to obtain experimentally or computationally.^{5–7,10–16,30–46} Part of the reason for this difficulty is that the interface energy is expected to vary with precipitate size and composition, both of which are somewhat difficult to unambiguously define for small clusters containing only a few oxygen atoms. In the present study, we adopt a hybrid

approach in which we propose a parameterizable functional form for the interface free energy based on atomistic simulation results and then employ model regression to a set of wafer annealing experiments to fit the parameters. We show that the resulting model can capture many of the key aspects of oxide precipitation under diverse conditions and then highlight the mechanisms responsible for some of the observations.

The remainder of the paper is organized as follows. The model details and associated background theory are presented in Sec. II. The experimental benchmark that was used to regress and assess the model is presented in Sec. III, along with details regarding the model global regression approach used in this study. Comparisons between the model and experimental benchmark are described in Sec. IV. Next, a mechanistic analysis of some of the key observations is discussed in Sec. V. Finally, conclusions are presented in Sec. VI.

II. THEORY AND METHODS

In this section, we present the various elements that comprise the overall model for oxygen precipitation. First, we present the overall balance equations for native point defects, interstitial oxygen atoms, voids, and oxide clusters and then describe in detail the various components of the free energy model for oxygen precipitates.

A. Overall balance equations for precipitates and point defects

The balance equations for interstitial oxygen (O), vacancies (V), and self-interstitials (I) are

$$\left(\frac{\partial}{\partial t} + v \frac{\partial}{\partial z}\right) C_O = D_O \frac{\partial^2 C_O}{\partial z^2} + \left(\frac{\partial}{\partial t} + v \frac{\partial}{\partial z}\right) \times \left[\int_2^{n_O^d} n C_O(n) dn_O + \int_{n_O^d+1}^{n_O^{\max}} n f_O(n) dn_O \right], \quad (1)$$

$$\begin{aligned} \left(\frac{\partial}{\partial t} + v \frac{\partial}{\partial z}\right) C_V = D_V \frac{\partial^2 C_V}{\partial z^2} - k_{IV}(C_I C_V - C_I^{eq} C_V^{eq}) + \left(\frac{\partial}{\partial t} + v \frac{\partial}{\partial z}\right) & \left[\int_2^{n_V^d} n C_V(n) dn_V + \int_{n_V^d+1}^{n_V^{\max}} n f_V(n) dn_V \right] \\ + \left(\frac{\partial}{\partial t} + v \frac{\partial}{\partial z}\right) & \left[\int_2^{n_O^d} n \gamma_V(n) C_O(n) dn_O + \int_{n_O^d+1}^{n_O^{\max}} n \gamma_V(n) f_O(n) dn_O \right], \end{aligned} \quad (2)$$

and

$$\left(\frac{\partial}{\partial t} + v \frac{\partial}{\partial z}\right) C_I = D_I \frac{\partial^2 C_I}{\partial z^2} - k_{IV}(C_I C_V - C_I^{eq} C_V^{eq}), \quad (3)$$

where D_i are monomer species diffusivities, C_i^{eq} are the equilibrium concentrations/solubilities, v is the velocity of the solid (zero for wafer

annealing experiments but finite for crystal growth²⁹), and k_{IV} is the interstitial-vacancy recombination rate constant. The terms containing integrals in the oxygen and vacancy balance equations represent monomer exchange with a size distribution of clusters, where $C_i(n)$ is the concentration of i -clusters of size n that are represented discretely,^{29,47} $f_i(n)$ is the concentration of (larger) i -clusters represented by a continuous size variable,^{29,47} n_i^d is the transition size between discrete

and continuous representations of the i -clusters—in the following, $n_i^d = 30$ for both vacancy and oxygen clusters. In Eq. (3), $\gamma_v(n)$ is the number of vacancies absorbed/emitted by oxygen clusters per oxygen atom; further details regarding this parameter are provided below.

All vacancy and oxide clusters ($n \geq 2$) are assumed to be immobile and can grow/dissolve only by monomer association/dissociation, i.e.,

$$\cdots \leftrightarrow n-1 \xrightleftharpoons[d(n)]{g(n-1)} n \xrightleftharpoons[d(n+1)]{g(n)} (n+1) \leftrightarrow \cdots, \quad (4)$$

where $g(n)$ and $d(n)$ are the growth and dissolution rates, respectively, of clusters of size n . The discrete cluster balance equations are written as Master equations,

$$\left(\frac{\partial}{\partial t} + v \frac{\partial}{\partial z}\right) C_i(n) = J_i(n) - J_i(n+1) \quad (n_i \leq n_i^d), \quad (5)$$

where $J_i(n)$ is the net flux between i -clusters of size n and $n+1$, i.e., $J_i(n) = g_i(n)C_i(n) - d_i(n+1)C_i(n+1)$. For cluster sizes larger than n_i^d , the Master equations are combined into a Fokker-Planck equation using a discrete-to-continuous size transformation; see Refs. 16, 47, and 48. The resulting balance equations are

$$\left(\frac{\partial}{\partial t} + v \frac{\partial}{\partial z}\right) f_i(n) = -\frac{\partial I_i(n)}{\partial n}, \quad (6)$$

where

$$I_i(n) = -B_i(n) \frac{\partial f_i}{\partial n} + A_i(n) f_i(n), \quad (7)$$

$$A_i(n) = g_i(n) - d_i(n) - \frac{\partial B_i(n)}{\partial n}, \quad (8)$$

and

$$B_i(n) = \frac{g_i(n) + d_i(n)}{2}. \quad (9)$$

Expressions for the growth and dissolution rates are given by assuming that the monomer field around an oblate spheroid cluster is a steady-state diffusion-limited one,⁸ i.e.,

$$g_i(n) = 4\pi R_p \frac{\sqrt{1-\beta^2}}{\cos^{-1}(\beta)} \beta^{-1/3} D_i C_i \quad (10)$$

and

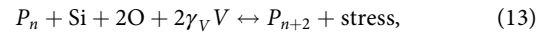
$$d_i(n) = 4\pi R_p \frac{\sqrt{1-\beta^2}}{\cos^{-1}(\beta)} \beta^{-1/3} D_i C_i^{GT}(n), \quad (11)$$

where β is the (size-dependent) aspect ratio of the oblate spheroid and $C_i^{GT}(n)$ is the Gibbs-Thomson concentration of monomers around an i -cluster of size n , which reflects the thermodynamic cost of forming the cluster,¹⁶ i.e.,

$$C_i^{GT}(n) = C_i^{eq} \exp\left(\frac{\partial G_i^f(n)/\partial n}{k_B T}\right). \quad (12)$$

B. Free energy models for oxide precipitates

The thermodynamic model for voids has been described previously in Ref. 21. Here, we describe the various components of the free energy model for oxide precipitates, which are assumed to be comprised exclusively of amorphous SiO_2 and which interact exclusively with vacancy point defects for stress modulation. Accordingly, the oxide precipitation process is schematically represented here by



in which a precipitate, P , containing n oxygen atoms grows by “oxidizing” one matrix silicon atom with two oxygen atoms to create a unit of SiO_2 and then partially relaxing the resulting stress by absorbing, at the matrix-precipitate interface, γ_v vacancies per oxygen atom ($2\gamma_v$ in total). Note that the process of vacancy absorption is thermodynamically equivalent to emitting a silicon interstitial at the precipitate-matrix interface. The equivalency arises because of the process of interstitial-vacancy recombination in the bulk matrix, $I + V \rightarrow \text{Si}$. Also, note that although we do not consider here the kinetics of point defect recombination in the context of oxide precipitation, self-interstitial emission and vacancy absorption are equivalent in practice only if recombination is fast relative to the oxide precipitation process. In other words, we consider vacancy absorption as the only point defect-mediated stress relief mechanism.

The free energy of an oxide precipitate is assumed to be comprised of three contributions, chemical, mechanical, and interfacial, i.e.,

$$G(n) = G^c(n) + G^s(n) + G^i(n). \quad (14)$$

The chemical energy, G^c , which represents the thermodynamic driving force resulting from super- or undersaturation of oxygen atoms and vacancies, is given by

$$G^c = -nk_B T \ln \frac{C_O}{C_O^{eq}} - n\gamma_v k_B T \ln \frac{C_V}{C_V^{eq}}. \quad (15)$$

In Eq. (15), the two terms represent the difference between the chemical potential of oxygen atoms and vacancies, respectively, in the matrix and oxide cluster phase. The strain energy, G^s , is described using a continuum mechanical model,⁴⁹ and is given by

$$G^s(n) = \frac{1}{2} \Delta V^2 \frac{K^* \varphi(\beta)}{K^* + \varphi(\beta)} V_p, \quad (16)$$

where

$$\Delta V = \frac{V_{\text{SiO}_2} - (V_{\text{Si}} + 2\gamma_v V_{\text{Si}})}{V_{\text{Si}} + 2\gamma_v V_{\text{Si}}} \quad (17)$$

and

$$\varphi(\beta) = \frac{K[(S_{1111} + S_{1122} - 1)(1 - S_{3333}) + 2S_{1133}S_{3311}]}{(S_{1111} + S_{1122} - 1)\left(S_{3333} - \frac{2}{3}\right) + 2(S_{3333} - S_{1133} - S_{3311} - 1)/3 - 2S_{1133}S_{3311}}. \quad (18)$$

In the preceding expressions, V_p is the volume of the precipitate, V_{Si} and V_{SiO_2} are the volume of Si and SiO_2 , respectively, on a per Si atom basis, K and K^* are the bulk moduli of the silicon matrix and oxide precipitate phases, β is the aspect ratio of the (oblate spheroidal) oxide precipitate, and S_{ijlm} is the Eshelby tensor for a spheroidal precipitate in a cubic symmetric silicon matrix;^{50–52} see the Appendix. Finally, the matrix-precipitate interfacial free energy, G^i , is given by

$$G^i(n) = \pi R_p^2 \left(2 + \frac{\beta^2}{\sqrt{1-\beta^2}} \ln \left(\frac{1 + \sqrt{1-\beta^2}}{1 - \sqrt{1-\beta^2}} \right) \right) \times \beta^{\frac{2}{3}} \left(\frac{1 + e_C}{1 + Xe_C} \right)^2 \sigma_O(n), \quad (19)$$

where e_C is the constrained strain, $X = 1 + 4\mu/3K$ and μ is the shear modulus of Si. The effective interface energy, σ_O , which may depend on the precipitate size and other variables, is the primary fitting function in this study.

Within the context of the free energy model described above, we assume that all clusters are able to achieve equilibrium rapidly with respect to their local environment. In other words, for each cluster size, the total free energy is always minimized with respect to its shape and vacancy content, given the local point defect and oxygen concentration,

$$\begin{aligned} \frac{\partial G(n, \gamma_V, \beta)}{\partial \gamma_V} &= 0, \\ \frac{\partial G(n, \gamma_V, \beta)}{\partial \beta} &= 0. \end{aligned} \quad (20)$$

The minimization, which is implemented numerically, is constrained

according to

$$\begin{aligned} 0 &\leq \gamma_V \leq 0.5, \\ 0 &\leq \beta < 1. \end{aligned} \quad (21)$$

Note that the upper bound on the vacancy fraction is determined as the vacancy fraction, γ_V , that enables a cluster to become fully relaxed.

III. EXPERIMENTAL DATABASE AND MODEL REGRESSION APPROACH

A benchmark consisting of multiple wafer thermal annealing experiments⁵³ was used to establish the prediction capability of our continuum oxide precipitation model. The overall structure of the thermal history profile used in these experiments is shown in Fig. 1. Wafers are subjected to an initial RTA temperature between 1100 and 1250 °C for 30 s after which the temperature is rapidly decreased to 500 °C at a rate of 75 K/s. The rapid temperature decrease creates a large supersaturation of native point defects, some of which mutually annihilate via interstitial-vacancy recombination. Subsequently, the temperature is ramped up at a rate of 100 K/min up to a nucleation temperature ($650^\circ\text{C} < T_{\text{nuc}} < 1000^\circ\text{C}$) for 4–16 h. The nucleation anneal serves to nucleate small oxide precipitates at relatively low temperatures, where both oxygen and vacancies are supersaturated and therefore precipitate free energies are low across all sizes.^{6,11,12,15} Once precipitate nucleation has proceeded for several hours, a 3-hour so-called “stabilization anneal” at 780 °C is applied in certain cases. The stabilization anneal serves to expose precipitates to an intermediate temperature, where precipitate growth is thermodynamically favorable across much of the size range. As the precipitates nucleated in the previous step grow, they become increasingly stable at higher temperatures. Finally, the 16-hour growth anneal at 1000 °C,

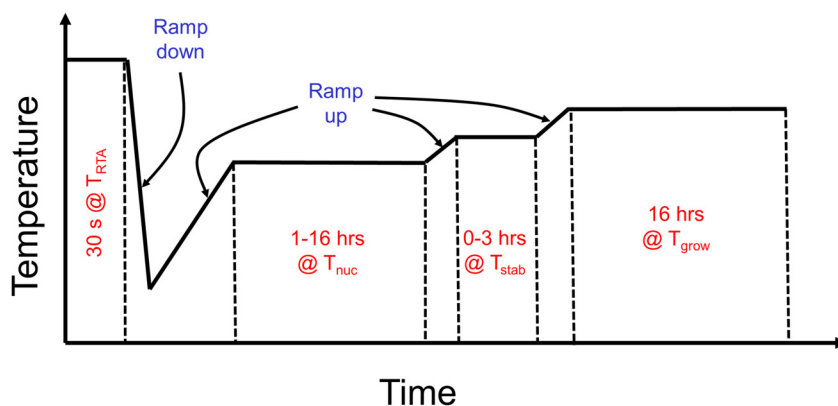


FIG. 1. Schematic of thermal history profile for wafer annealing experimental benchmark.

TABLE I. Experimental benchmark based on wafer thermal annealing and subsequent oxide precipitate density measurements for model regression.⁵³

Experiment index	T_{RTA} (°C)	T_{NUC} (°C)	T_{STAB} (°C)	Prec. density (cm ⁻³)
1	1200	800/8 h	NA	7.57×10^9
2	1175	700/8 h	NA	4.34×10^8
3	1200	1000/8 h	NA	8.18×10^7
4	1250	800/8 h	NA	1.97×10^{11}
5	1250	1000/8 h	NA	4.50×10^{10}
6	1100	800/8 h	NA	1.00×10^7
7	1100	700/8 h	NA	3.58×10^7
8	1100	700/16 h	NA	1.18×10^9
9	1100	700/8 h	780/3 h	5.57×10^8
10	1100	700/16 h	780/3 h	4.00×10^{10}
11	1100	650/4 h	780/3 h	5.17×10^8
12	1100	650/8 h	780/3 h	1.37×10^{10}
13	1100	650/16 h	780/3 h	5.87×10^{10}

where oxygen diffusion is enhanced, serves to grow all stable precipitates to measureable sizes.

The conditions of the 13 wafer annealing experiments are summarized in Table I. In simulating these experiments, we assume that no oxygen precipitates initially exist in the as-grown material and that the wafer thickness is 0.725 mm. We also take the initial oxygen concentration to be fixed at $6.5 \times 10^{17} \text{ cm}^{-3}$. The estimated uncertainty in the oxide precipitate density is a factor of two on either side of the reported values in Table I.

A. Summary of known parameters

The overall oxygen precipitation model described in Sec. II requires the specification of a large number of thermophysical properties for point defects, interstitial oxygen, vacancy aggregates, and oxide precipitates. Many of these parameters have been established over the years using both experimental and computational studies.^{26–29} In this section, we list model parameters that are assumed to be known and therefore fixed throughout the present study. First, the equilibrium concentration, or solubility limit, of interstitial oxygen atoms, O_i , is taken from the work of Mikkelsen,²⁶ i.e.,

$$C_O^{\text{eq}} = 9 \times 10^{22} \exp\left(\frac{-1.52 \text{ eV}}{k_B T}\right) \text{ cm}^{-3}. \quad (22)$$

The diffusivity of O_i at temperatures greater than 700 °C has been established at²⁶

$$D_O = 0.13 \times \exp\left(\frac{-2.53 \text{ eV}}{k_B T}\right) \text{ cm}^2/\text{s}, \quad (23)$$

while the diffusivity below 700 °C is given by²⁷

$$D_O = 7.33 \times 10^{-7} \exp\left(\frac{-1.52 \text{ eV}}{k_B T}\right) \text{ cm}^2/\text{s}. \quad (24)$$

Native point defect equilibrium concentrations and diffusivities used here are based on recently revised estimates using a large database of crystal growth experiments.²⁹

$$C_V^{\text{eq}} = 4.97 \times 10^{22} \exp(8.29) \exp\left(\frac{-3.86 \text{ eV}}{k_B T}\right) \text{ cm}^{-3}, \quad (25)$$

$$C_I^{\text{eq}} = 2.97 \times 10^{23} \exp(8.47) \exp\left(\frac{-4.23 \text{ eV}}{k_B T}\right) \text{ cm}^{-3}, \quad (26)$$

$$D_V = 0.00021 \times \exp\left(\frac{-0.30 \text{ eV}}{k_B T}\right) \text{ cm}^2/\text{s}, \quad (27)$$

and

$$D_I = 0.223 \times \exp\left(\frac{-0.72 \text{ eV}}{k_B T}\right) \text{ cm}^2/\text{s}. \quad (28)$$

The thermodynamic model for the void surface free energy used here is based on the model described in Ref. 21. Finally, the following mechanical properties are assumed: the bulk modulus (K^*) of oxide precipitates is 34.7 GPa,⁵⁴ while the shear (μ) and bulk (K) moduli of the silicon crystal matrix are 64.1 GPa¹⁶ and 97.8 GPa,⁵⁵ respectively. Given that the annealing temperatures in Table I are well below the melting point of silicon (and SiO_2), these properties are assumed to be independent of temperature.

B. Model regression strategy

The goal of the global regression is to find a combination of the parameters that describe the interface energy function (see Sec. IV) that minimize the difference between the predicted and experimental oxide precipitate densities for the experimental wafer annealing benchmark in Table I. The optimization is subject to the semiquantitative constraints that (1) no visible oxide precipitates (i.e., size <20–40 nm)^{56,57} are predicted to form during crystal growth and (2) predicted void size distributions in as-grown CZ crystals are consistent with previous findings.⁵⁸ The objective function used in our study is given by

$$OF = \frac{100}{n} \sum_{x=1}^n \left| \frac{C_x^{\text{sim}} - C_x^{\text{exp}}}{C_x^{\text{sim}} + C_x^{\text{exp}}} \right|^\alpha, \quad (29)$$

where C_x^{exp} is the measured oxide precipitate density listed in Table I for benchmark index x , C_x^{sim} is the corresponding simulation result, n is the number of experiments in the benchmark ($n = 13$ in the present study) and α is a nonlinearity factor for tuning the deviation penalty. In order to account for the uncertainty in the experimental data in Table I, a value of $\alpha = 6$ is used for all optimizations, which effectively “flattens” the objective function around the target values. We note here that the crystal growth constraints mentioned above were not directly included into the objective function, principally because of computational costs associated with performing the required calculations to assess constraint violation. This issue is discussed further in Sec. IV.

In search of a global minimum of Eq. (29), we considered genetic and other population-based optimization algorithms. In particular, we compared three different population-based optimization approaches: (1) a simple differential evolution (DE) algorithm,⁵⁹ (2) a homogenous islands model employing the DE1220 algorithm,⁶⁰ and (3) a heterogeneous islands model employing a mixture of different algorithms executed concurrently.^{61–63} The latter two island approaches, performed using the PaGMO package,⁶⁰ represent a coarse-grained parallel approach to global optimization, with the benefit of increased robustness in finding the global optimum, particularly if several optimization algorithms are used simultaneously. In order to achieve reasonable computational performance, the calculations were parallelized over all benchmark cases and distributed over several nodes of a compute cluster using standard software (GNU Parallel).⁶⁴ Typical solution times for one complete objective function evaluation varied significantly, from about 10 s to more than 600 s.

Optimizer evolution trajectories for the 8-parameter interface free energy function discussed in Sec. IV B are shown in Fig. 2. A fully parallelized, single-population DE algorithm (algorithm 1 in Fig. 2) converged relatively quickly to an intermediate local minimum solution (OF ~ 8) but did not progress further; we refer to this parameter combination as “Model 1.” The 8-island homogeneous archipelago (algorithm 3) at first seemed relatively inefficient in that it attains a similar minimum OF value to that found by simple DE but took longer to do so. However, closer inspection shows that it had made a few excursions into a new area of parameter space with lower OF when it was halted. The best performance was clearly achieved with the 12-island mixed archipelago (algorithm 2), which showed rapid evolution from the OF ~ 8 basin to another located at OF ~ 3 —the latter is believed to be the global minimum and is denoted as “Model 2.” The physical significance of the interface free energy functions that correspond to “Model 1” and “Model 2” is discussed in Sec. IV.

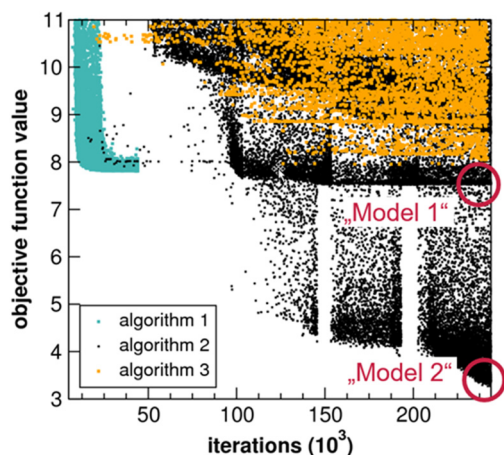


FIG. 2. Optimization history for three different optimization approaches: (1) single population of size 100 evolved with DE, (2) 12 islands of size 20 evolved with 7 different algorithms, (3) 8 islands of size 20 evolved with DE1220.

IV. RESULTS AND DISCUSSION

A. Constant surface energy model

A single-parameter, constant Si/SiO₂ interface energy model was considered first to assess the ability of the experimental benchmark to discriminate between different models. We find an optimal fit at $\sigma_o = 1.02 \text{ J/m}^2$; see Fig. 3. While some of the general trends are captured across the benchmark, there are also some notable deviations between the model predictions and the experimental data. For example, the model largely fails to capture the precipitate density variations when the RTA temperature is low (benchmarks #6–#13). Recall that this group of annealing experiments corresponds to the situation in which a low vacancy supersaturation is produced following the initial RTA step—these conditions correspond to increased precipitate stress and generally slower rates of growth. Consequently, the impacts of nucleation time and temperature become more significant, as reflected by the experiments—but not the simulations with constant surface energy. In summary, a single-parameter model is insufficient to adequately describe the oxide precipitation process during wafer thermal annealing.

B. Generalized surface energy model

The failure of the single-parameter interface energy model considered in Sec. IV A indicates that a more complex function (with additional regression parameters) is required to capture the various features of the experimental benchmark. Although the introduction of additional parameters automatically increases the fitting capacity, here we employ the results of recent electronic structure calculations to propose a physically justifiable surface energy model. Shown in Fig. 4(a) are the results of electronic structure atomistic calculations for the formation energies of various (small) V_nO_m clusters containing m oxygen atoms and n vacancies; the results are taken from

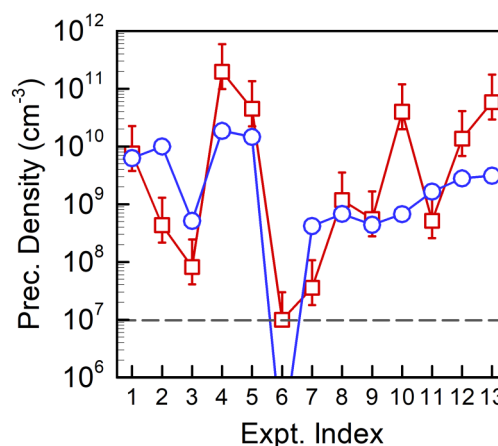


FIG. 3. Oxide precipitate density prediction using a constant surface energy model for the 13-experiment benchmark; optimum surface energy is 1.02 J/m^2 . Red squares—experimental measurements (errors indicate an uncertainty of a factor of 2), blue circles—optimized simulation. The horizontal dashed line represents an estimate of the experimental detection threshold.

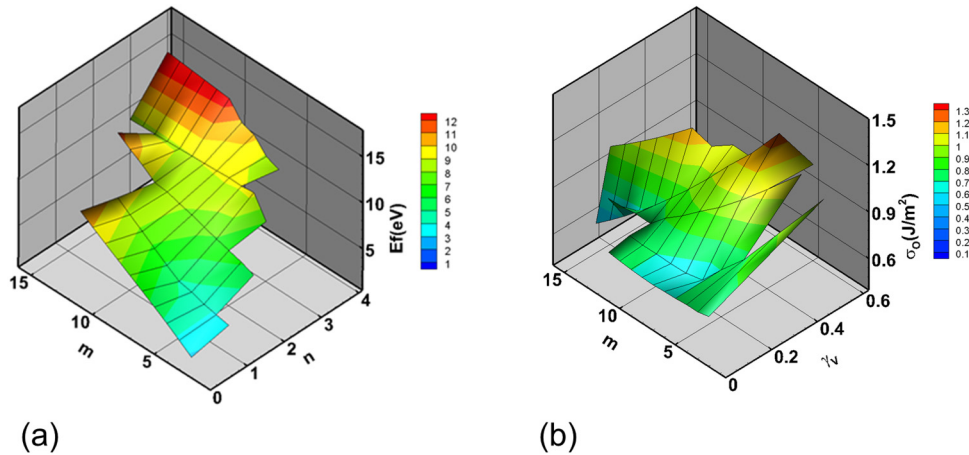


FIG. 4. (a) Vacancy-containing oxygen cluster formation energies predicted by electronic structure calculations described in Ref. 65. (b) Effective oxygen precipitate interface free energy obtained by interpreting the energies in (a) with Eq. (27). Adapted with permission from G. Kissinger *et al.*, J. Cryst. Growth **468**, 424 (2016).⁶⁵

Ref. 65. As expected, the formation energy rises as the number of oxygen atoms in the cluster increases across the range of sizes considered. By contrast, increasing the vacancy content for a given number of oxygen atoms initially seems to have little impact on the formation energy but eventually strongly increases it.

Based on these data alone, trends are difficult to extrapolate to larger cluster sizes and the high computational cost of performing electronic structure calculations strongly limits the range of sizes that may be considered in this way. We address this limitation by interpreting the data shown in Fig. 4(a) in terms of the continuum free energy model for oxygen precipitates. Cluster formation energies were inserted into the left-side of Eq. (27), and then assuming that (1) interstitial oxygen and vacancies were at their equilibrium concentrations and (2) all clusters are spherical in shape ($\beta = 1$), an effective Si/SiO₂ interface energy was obtained as a function of oxygen cluster size and vacancy fraction, i.e.,

$$E^f(n, m) = \frac{1}{2} \Delta V^2 \frac{K^* \varphi(\beta = 1)}{K^* + \varphi(\beta = 1)} V_p + \pi R_p^2 \left(\frac{1 + e_c}{1 + X e_c} \right)^2 \sigma_O^{\text{eff}}, \quad (30)$$

with cluster radius, $R_p = (3V_p/4\pi)^{1/3}$, and constrained strain, $e_c = [(2/(1 + 2\gamma_V))^{1/3} - 1]/X$, respectively. The results of this procedure are shown in Fig. 4(b). Most obviously, the effective interface energy appears to decrease monotonically with the number of oxygen atoms, presumably toward some large-limit continuum value that is lower than 1 J/m². The larger effective interface energy of very small clusters (~ 1.2 – 1.5 J/m²) may be interpreted qualitatively in the context of a Tolman-type correction,^{66–68} which accounts for the effect of curvature on the interface energy between two phases. In addition to the apparent dependence on cluster size, the interface free energy is also seen to depend strongly on the vacancy fraction, γ_V , increasing as the vacancy fraction increases. This behavior suggests that incorporation of vacancies into an oxide precipitate as a mechanism of relaxation is a balance between increasing surface energy and lower stress.

It is worth placing these interface free energy values in the context of prior studies. Generally, there are three types of estimates for the Si/SiO₂ interface free energy in the literature: (1) “direct” measurements of Si/SiO₂ interface energies created by wafer bonding,^{30–36} (2) atomistic simulations,^{37–43} and (3) model regression to oxide precipitation experiments in annealed wafers. Overall, the direct measurements show the widest range but seem to suggest that fully “healed” interfaces are high in energy (~ 2.5 J/m²), although it is not necessarily clear that these interfaces correspond to oxide precipitate-matrix interfaces formed by bulk oxygen precipitation. Interestingly, it is the plasma-treated cases^{31,32} that generally provide values near the upper end of the range—most of the cases without this treatment tend to lead to values in the range 1–1.5 J/m². It may, therefore, be the case that the plasma treatment somehow alters the interface in a way that does not correspond to spontaneous oxide precipitation in the Si bulk. Atomistic simulations suggest values in the range 0.8–1.5 J/m². Much of the scatter in this data is likely to be the result of a combination of two factors: (1) error in the potential models used to compute the energy and (2) insufficient annealing of the interface. It is also interesting to note that the atomistic simulation results are quite consistent with the direct experimental measurements (for the nonplasma treated cases). Finally, the oxide precipitate model fitting literature appears to provide interface energies that are generally lower: 0.2–0.7 J/m², although some studies provide outlier values.^{11,12} Overall, there is a suggestion that the oxide precipitate models prefer interface energy values that are significantly lower than those obtained by either atomistic simulations or direct measurement.

Based on the observations in Fig. 3, we propose an 8-parameter interface free energy model of the form

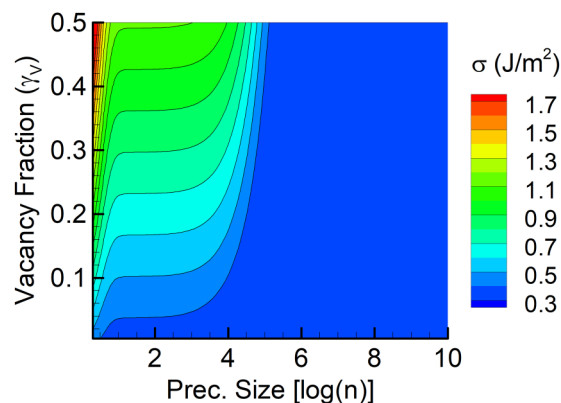
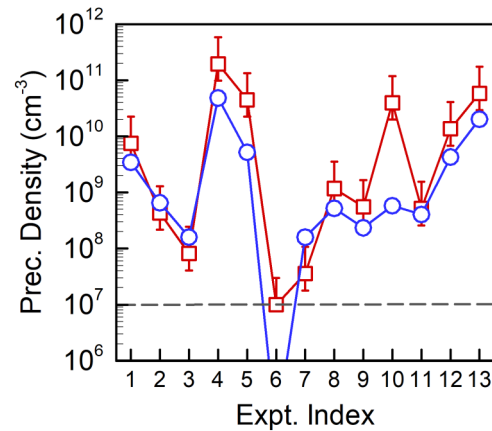
$$\sigma_O(m, \gamma_V) = v_1 + \left(v_2 + \frac{v_3 \gamma_V}{0.5} \right) \exp \left(\frac{-5m}{v_4(1 + 2\gamma_V v_5)} \right) + \left(v_6 + \frac{v_7 \gamma_V}{0.5} \right) \exp \left(\frac{-5(m-2)}{v_8 - 2} \right), \quad (31)$$

TABLE II. Parameter set “Model 1” for Si/SiO₂ interface free energy model in Eq. (31). See text for details.

v_1	v_2	v_3	v_4	v_5	v_6	v_7	v_8
0.301	0.0418	0.771	7217	41.2	0.097	0.771	10.6

where v_1 is the limiting interface energy per unit area for large clusters. The second term, with fitting parameters $\{v_2-v_5\}$, represents a decay function for larger clusters. The third term, which includes the fitting parameters $\{v_6-v_8\}$ represents a “lip” function that is applied for small clusters. The 8-parameter interface model in Eq. (31) was regressed to the experimental benchmark using the global optimization approaches described in Sec. III B. Several distinct parameter sets were identified that led to good representation of the benchmark; we discuss two of them here. The first parameter set, “Model 1,” is listed in Table II, while the corresponding interface energy function is plotted in Fig. 5. Recall that Model 1 corresponds to a local minimum (OF ~ 8) found by all three optimization approaches described in Sec. III B. The small-cluster penalty is clearly visible for sizes smaller than about 20 oxygen atoms, followed by an intermediate size region up to $n = 10^4$, and finally a large-size limit where the interface energy becomes constant at a value of 0.301 J/m².

The agreement between simulation and experiment is generally very good across the benchmark, Fig. 6. In particular, the effects of RTA temperature and the nucleation annealing time are both captured well, unlike in the case of the constant interface energy model. However, significant deviations between the simulations and experiments do exist for 2 cases, #6 and #10. In the case of benchmark #6, it should be noted that the experimental measurement is close to the oxide precipitate density detection threshold ($\sim 10^7$ cm⁻³); i.e., it is possible that the actual precipitate density is substantially lower than the reported value. Consequently, the experimental value may be considered to be an upper bound and the fact that the simulations predict a much lower value may not indicate a meaningful discrepancy.

**FIG. 5.** Oxide precipitate surface energy as a function of precipitate size and vacancy fraction as represented by the best fit of Eq. (31) to the experimental benchmark.**FIG. 6.** Oxide precipitate density prediction with the optimized interface free energy model in Eq. (31) for the 13-experiment benchmark; corresponding model parameters are shown in Table II. Red squares—experimental measurements (errors indicate an uncertainty of a factor of 2), blue circles—simulation. The horizontal dashed line represents an estimate of the experimental detection threshold.

Although not considered explicitly in the global regression approach, meaningful predictions of oxide precipitate and void formation during bulk crystal growth also are required for a parameter set to be considered valid (see Sec. III B). Shown in Fig. 7 are the predicted oxide precipitate and void densities using the same parameters for an 8-in. diameter CZ crystal grown under vacancy-rich conditions; additional details of the crystal growth conditions are provided in Ref. 58. The predicted oxide precipitate size distribution (solid curves) shows a high concentration of very small clusters that

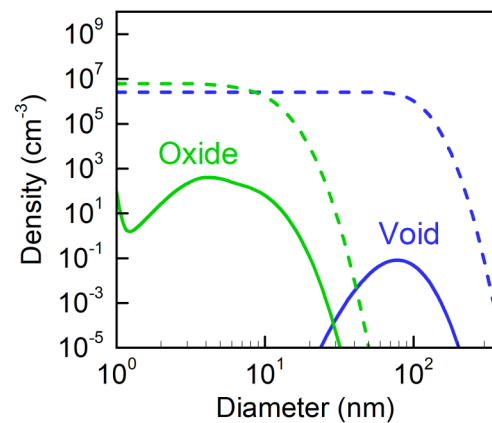
**FIG. 7.** Density of oxide precipitates (green) and voids (blue) as a function of precipitate diameter predicted for a CZ-grown crystal using the “Model 1” Si/SiO₂ interface free energy parameters described in Table II. Solid and dashed curves represent the size distribution and integrated density across detectable sizes, respectively. The crystal thermal field and pulling velocity correspond to case “8A” in Ref. 58.

TABLE III. Parameter set for Si/SiO₂ interface free energy model “Model 2.” See text for details.

ν_1	ν_2	ν_3	ν_4	ν_5	ν_6	ν_7	ν_8
0.687	0.151	−0.373	1660	−0.200	0.248	0.753	6.41

would be invisible without further precipitate growth annealing⁵⁸ and a very low (undetectable) density of large precipitates. In other words, the simulation predicts that no oxide precipitates would be visible in the as-grown crystal—in agreement with experimental observations. The simulated void density distribution, when integrated (dashed curve) across all detectable sizes (diameters larger than about 30 nm) is $2.07 \times 10^6 \text{ cm}^{-3}$, which is in excellent agreement with previously reported measurements in the range⁵⁸ $1\text{--}2 \times 10^6 \text{ cm}^{-3}$. In summary, the Si/SiO₂ interface free energy model parameters in Table II provide a very good representation of the wafer annealing benchmark while simultaneously leading to predictions that are fully consistent with crystal growth experiments.

To demonstrate the importance of consistency across multiple types of experiments, we consider a second set of parameters (“Model 2,” parameters in Table III) that also provide good agreement with the wafer annealing benchmark. As shown in Fig. 8, the representation of the experimental benchmark is even better than the base case in Fig. 6, and, in fact, this case represents a lower objective function found by global optimization (OF ~ 3 as mentioned in Sec. III B). However, as shown in Fig. 9, this interface energy model leads to some obviously erroneous predictions for the crystal growth scenario—an observable distribution of oxide precipitates and no visible voids, both of which are inconsistent with experimental observations and correspond

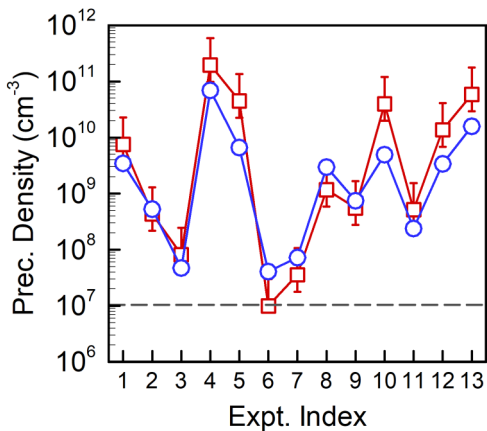


FIG. 8. Oxide precipitate density prediction with the optimized interface free energy model in Eq. (31) for the 13-experiment benchmark; corresponding model parameters are shown in Table III. Red squares—experimental measurements (errors indicate an uncertainty of a factor of 2), blue circles—simulation. The horizontal dashed line represents an estimate of the experimental detection threshold.

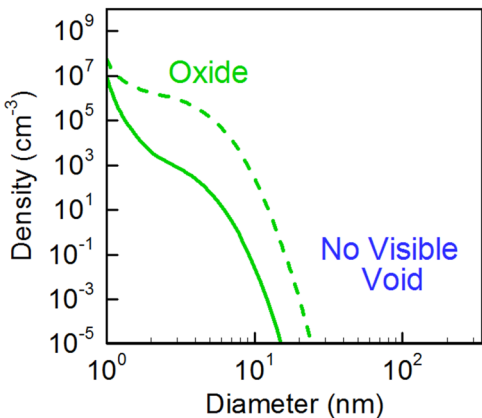


FIG. 9. Density of oxide precipitates (green) and voids (blue) as a function of precipitate diameter predicted for a CZ-grown crystal using the Si/SiO₂ interface free energy model parameters described in Table III. Solid and dashed curves represent the size distribution and integrated density across detectable sizes, respectively. The crystal thermal field and pulling velocity correspond to case “8A” in Ref. 58.

to “overly aggressive” oxide precipitate growth physics in which vacancies are sequestered into growing oxide precipitates before they can aggregate into voids.⁵⁸ In summary, the “Model 2” parameter set in Table III provides an excellent representation of the wafer annealing benchmark but a qualitatively incorrect prediction for crystal growth. This finding highlights the fact that the 13-experiment benchmark considered here, although quite comprehensive in terms of the annealing conditions it includes, is not sufficient alone for the identification of a valid Si/SiO₂ interface model. Moreover, the parameters in Table III correspond to an effective interface free energy that decreases with increasing vacancy content, in qualitative disagreement with the atomistic results shown in Fig. 5.

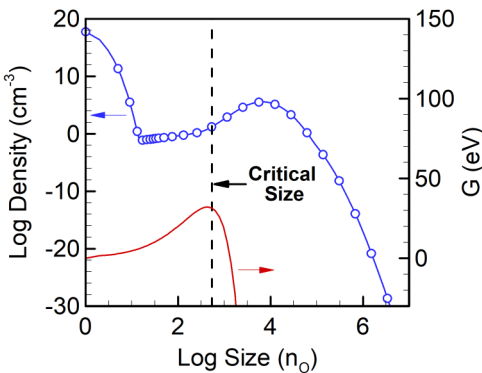


FIG. 10. Snapshot in time of the oxide precipitate size distribution (blue curve), precipitate free energy (red curve), and critical precipitate size (black dashed line), at $t = 29\,140$ s for benchmark #1.

V. MECHANISTIC ANALYSIS OF OXIDE PRECIPITATION

A key feature of oxide precipitation across the benchmark is the sensitivity of the final precipitate density to various aspects of the annealing process, such as the RTA temperature and the nucleation time. This sensitivity is generally difficult to capture well in simulation and therefore a detailed analysis of how it arises is warranted. We analyze the evolution of oxide precipitates by considering the size distribution along with the precipitate free energy—both quantities evolve in time during all stages of the annealing process. Shown in Fig. 10 is an example snapshot ($t = 29\,140$ s, benchmark #1) of

the oxide precipitate size distribution (blue curve with circles) and precipitate free energy as a function of size computed using Eq. (32) (red curve). Also marked on the figure is the critical precipitate size at that time, which corresponds to the size at which the free energy is maximal, denoted by the vertical black dashed line. Note that a good approximation of the cluster nucleation rate is given by the cluster density at the critical size.^{13,69} During annealing, the critical size generally is most strongly impacted by the evolving oxygen and vacancy supersaturations. In the following discussion, the density of stable clusters is defined as all clusters that are larger than the

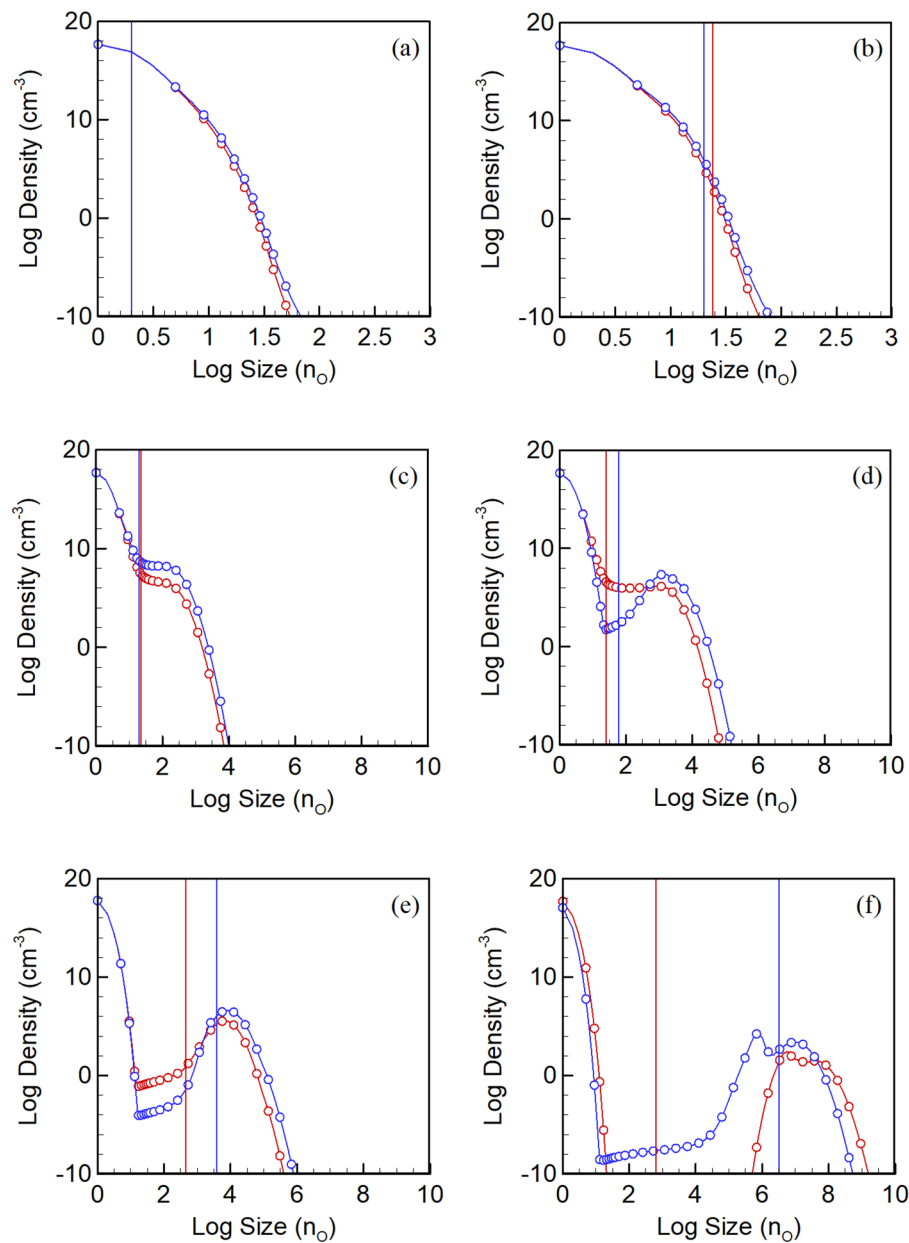


FIG. 11. Oxide precipitate size distribution (curves with symbols) and critical size (vertical line) at (a) $t = 40$ s ($T = 500$ °C), (b) $t = 220$ s ($T = 800$ °C), (c) $t = 2220$ s ($T = 800$ °C), (d) $t = 10\,220$ s ($T = 800$ °C), (e) $t = 29\,140$ s ($T = 1000$ °C), and (f) end of anneal, $t = 86\,739$ s ($T = 1000$ °C). Red— $T_{\text{RTA}} = 1200$ °C (benchmark #1); blue— $T_{\text{RTA}} = 1250$ °C (benchmark #4).

current critical size, i.e.,

$$C^{\text{stab}} = \int_{n_{\text{crit}}}^{n_{\text{max}}} C(n) dn. \quad (32)$$

A. Impact of RTA temperature on oxide precipitate density

The final precipitate densities in benchmarks #1 and #4 differ by almost two orders-of-magnitude despite being nearly identical in thermal history, with the exception that $T_{\text{RTA}} = 1200^\circ\text{C}$ for benchmark #1 and $T_{\text{RTA}} = 1250^\circ\text{C}$ for benchmark #4. We analyze this high sensitivity to RTA temperature by considering the temporal evolution of the precipitate size distribution and critical size for both cases. Shown in Fig. 11 is a sequence of snapshots of the oxide precipitate size distributions during the anneals. In both cases, immediately following the ramp-down from the RTA ($t = 40$ s), Fig. 11(a), a very high vacancy and oxygen supersaturation reduces the critical size to the smallest oxygen cluster (dimers). Although the lower RTA temperature in benchmark #4 (red curve) leads to a slightly lower cluster density, the difference is essentially negligible at this point. During the following ramp-up to the nucleation temperature, point defect and oxygen supersaturations decrease and the precipitate distribution begins to evolve rapidly. By the end of the ramp-up [Fig. 11(b), $t = 220$ s] small but measurable differences in critical size ($n_{\text{crit}} = 24$ for $T_{\text{RTA}} = 1200^\circ\text{C}$ and $n_{\text{crit}} = 20$ for $T_{\text{RTA}} = 1250^\circ\text{C}$) and precipitate size distribution are apparent. Most of the difference in critical size is due to the larger vacancy concentration installed at the higher RTA temperature. Although the differences appear to be relatively minor, the density of stable clusters, even at this very early time, already differs by over two orders-of-magnitude. This is a direct consequence of the higher nucleation rate for benchmark #4 (higher precipitate density at the critical size).

The evolution of the precipitate size distribution and critical size during the subsequent nucleation anneal at 800°C are shown in Fig. 11(c) ($t = 2220$ s) and (d) ($t = 10\,220$ s). At the earlier time, the critical sizes remain at the same values as those in Fig. 11(b). Later during the nucleation anneal [Fig. 11(d), $t = 10\,220$ s], enough oxide precipitates have formed to create significant vacancy depletion in benchmark #4 ($T_{\text{RTA}} = 1250^\circ\text{C}$). In fact, the larger precipitate density in benchmark #4 actually creates a vacancy undersaturation, while a weak supersaturation still persists in benchmark #1. Consequently, the critical size for benchmark #4 becomes larger than that for benchmark #1 ($n_{\text{crit}} = 60$ vs $n_{\text{crit}} = 24$). The effect of this reversal is a slight reduction in the difference in precipitate density between the two cases.

The last two snapshots in Figs. 11(e) and 11(f) show the evolution of the precipitate size distribution and critical size during the final growth anneal at 1000°C . At the beginning of the growth anneal [Fig. 11(e), $t = 291\,400$ s], the critical size for benchmark #1 is located at $n_{\text{crit}} \sim 300$, which is well separated from the peak of the size distribution at $n \sim 10^4$. Consequently, the production/destruction of stable nuclei is negligible. By contrast, the critical size in benchmark #4 is much larger ($n_{\text{crit}} \sim 3000$), again due to vacancy undersaturation, and is located near the density peak. Note that in both cases, the size distribution has evolved into the classical bimodal shape that includes a steady-state distribution of very small subcritical clusters that is well separated from a second peak

of much larger, supercritical precipitates that will continue to grow during the growth anneal. At the end of the growth anneal [Fig. 11(f), $t = 86\,739$ s], the peak precipitate density is located at $n \sim 10^{7-8}$ in both cases. While the larger density of stable clusters in benchmark #4 persists to the end of the growth anneal, the shape of the size distribution is impacted by the earlier vacancy depletion and large critical size, namely, in the form of a “double-peak” consisting of spherical and platelike precipitates.

B. Impact of duration of nucleation anneal on oxide precipitate density

The impact of nucleation anneal time also was studied mechanistically by comparing the precipitate evolution in benchmarks #11 and #13, which differ only in the amount of time spent at 650°C (4 h and 16 h, respectively), resulting in a 100-fold increase in precipitate density for benchmark #13 (see Table I). Note that both benchmarks correspond to low RTA temperature (1100°C), in which the post-RTA vacancy concentration is relatively small. Under these “conventional annealing” conditions, growing oxide precipitates must reduce stress by assuming more plateletlike shapes, rather than by absorption of vacancies. Consequently, precipitate nucleation is less “explosive” at early times and continues to proceed steadily during the nucleation anneal.

Shown in Fig. 12 is the total density of stable clusters for the two anneals as a function of time. After a monotonic increase in supercritical precipitate density, benchmark #11, labeled by the red curve, exhibits a steep drop ($\sim 99\%$ reduction) in stable cluster density at $t = 14\,528$ s, following the ramp-up to the stabilization anneal at 780°C after 4 h of nucleation annealing at 650°C (“a₁” to “b₁”). By contrast, the stable precipitate density continues to rise monotonically over the next 12 h of nucleation annealing in benchmark #13. By the time the ramp-up to the stabilization temperature takes place in benchmark #13 ($t = 57\,806$ s, “a₂”), the stable cluster density is higher ($\sim 4\times$ that of the value at 4 h) and, after the

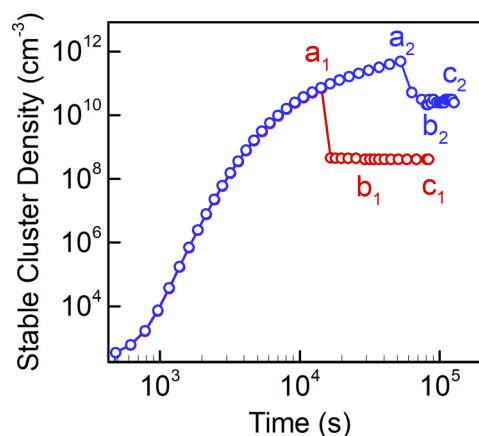


FIG. 12. Concentration of stable oxide precipitate clusters (those at or above the critical size) as a function of time. Red— $t_{\text{nuc}} = 4$ h (benchmark #11), blue— $t_{\text{nuc}} = 16$ h (benchmark #13).

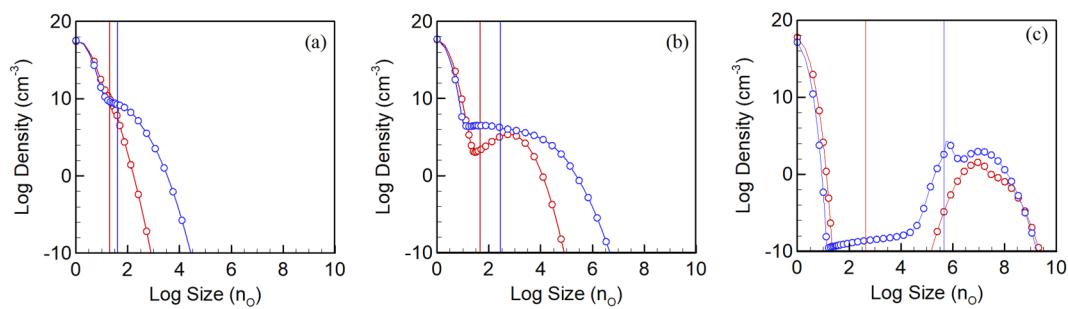


FIG. 13. Oxide precipitate size distribution and critical size (vertical lines) at points corresponding to labeled locations in Fig. 12. (a) Locations “a₁,” $t = 14\,528$ s (red) and “a₂,” $t = 57\,806$ s (blue); (b) locations “b₁,” $t = 25\,406$ s (red) and “b₂,” $t = 68\,606$ s (blue); (c) locations “c₁,” $t = 86\,138$ s (red) and “c₂,” $t = 126\,338$ s.

ramp-up (“b₂”), the extent of dissolution is lower (~90% instead of 99% dissolution). In both benchmarks, the total stable cluster density is largely unaffected by the remainder of the stabilization anneal and the subsequent growth anneal (“c₁” and “c₂”).

The precise extent of dissolution in each case is dictated by a complex interplay of several factors, including the temperature dependence built into the free energetic description for oxide clusters. In Fig. 13(a), the size distributions at “a₁” ($t = 14\,528$ s) and “a₂” ($t = 57\,806$ s) show that the additional 12 h of nucleation time only slightly increases the critical size (presumably because of vacancy undersaturation) while increasing the number of stable precipitates. However, the 3-hour stabilization anneal, Fig. 13(b), more significantly increases the critical size, particularly for benchmark #13 (40–280). As the temperature is increased to and held at the stabilization temperature, the critical size increases due to the explicit temperature dependence in Eq. (15). Interestingly, the equilibrium vacancy content (γ_v) of oxide clusters also increases from zero before the ramp-up to ~0.2 for clusters near the critical size (data not shown)—this effect arises from the vacancies supplied by the dissolving newly subcritical clusters. As shown previously in Figs. 4 and 5, the increase in γ_v increases the effective interface free energy, which would then be expected to further increase the critical cluster size. This mechanistic element for indirect temperature dependence of the surface energy may be contrasted with prior models that employed a direct but empirical temperature dependent interface free energy. Nonetheless, in spite of the increase of critical size shown in Fig. 13(b), the long nucleation anneal in benchmark #13 created precipitates of sufficient size so as to allow a large fraction of them to grow ahead of the increasing critical size. This trend continues until the end of the respective growth anneals [Fig. 13(c)]. The very large critical size for benchmark #13 is now mostly dictated by the significant depletion of oxygen atoms, in contrast to the benchmark #11 case, which does not create sufficient precipitation to strongly reduce the oxygen concentration. Once again, the critical size in benchmark #13 is large enough to intersect the peak of the precipitate distribution, creating a bimodal shape.

VI. CONCLUSIONS

The challenges associated with developing a quantitatively predictive model for oxide precipitation in bulk silicon are well

established. At the heart of the problem is the fact that oxide precipitation is a multifaceted and multiscale phenomenon that requires consideration of thermodynamics, kinetics, and mechanics at scales ranging from single atoms to tens of micrometers. While the overall phenomenology is at least qualitatively understood, enough details are still sufficiently murky that a parameter-free description remains elusive.

In this study, we proposed a hybrid approach in which well-understood phenomena and associated parameters were explicitly modeled while others were implicitly embedded into a multiparameter empirical function describing the effective interface free energy between an oxide precipitate and the surrounding Si crystal matrix. The dependence of this function on the precipitate size and vacancy fraction in the small size limit is designed to capture the impact of atomic discreteness, e.g., a nonsmooth interface, ambiguity in defining composition at the atomic scale, etc. In principle, this function is also able to embed other sources of model error in the small-cluster limit, including the continuum mechanical picture used to estimate precipitate stress and strain.

The regression of the effective interface free energy function to the wafer annealing benchmark used in the present study indicates that multiple parameter combinations are able to capture the benchmark. This observation highlights one of the potential pitfalls of model regression to experimental data—that of model sloppiness, described previously in models of biochemical reaction networks,^{70,71} whereby one or more of the parameters (or their combinations) are insensitive to the fitting data. We find that including additional qualitative constraints by considering oxide and void densities in as-grown crystals greatly reduces the number of admissible parameter candidate sets. Nonetheless, the experimental benchmark selected here appears to be quite diverse—a single-parameter (constant) interface energy model, commonly employed in previous models, is clearly shown to be inadequate for capturing the entire benchmark. Moreover, no good fits across the benchmark could be obtained without explicitly incorporating vacancy-content dependence in the effective interface free energy model for small clusters, i.e., size-dependence alone was insufficient. It is important to acknowledge that such effects are difficult to anticipate without atomistic-scale input such as the density functional theory (DFT) calculations used in the present work. Even so, the role of atomistic simulation in the context of oxide precipitation in silicon is yet to be fully explored. In particular, it remains an

open question as to whether computationally efficient empirical potentials are sufficiently accurate to more directly explore the thermodynamics and structures of small oxide precipitates.

Finally, it may be useful to consider more broadly the question of how to optimally resolve the physics of parameterizable oxide precipitation models along the spectrum that ranges from a complete physical description all the way to a “physics-free” black box, such as a neural network. If the end goal is simply to obtain a practical tool for predicting oxide precipitate density and size distributions for a given thermal anneal, the physical complexity of oxide precipitation, along with the availability of experimental training data, may very well justify the use of the latter. In either case, future work will obviously benefit from larger, more diverse experimental benchmarks for both regression and validation.

ACKNOWLEDGMENTS

We gratefully acknowledge Siltronic AG for partial financial support of this work and Dr. Gudrun Kissinger for valuable discussions regarding the energetics of small oxide clusters.

APPENDIX: INTERNAL STRAIN FIELD OF AN OBLATE SPHEROIDAL INHOMOGENEITY

The analytical expression for the elastic stress inside an oblate spheroidal inhomogeneity in an anisotropic matrix can be obtained by using the theory of Lee and Johnson,^{49,72} which is derived under the general framework of the equivalent inclusion method.^{50–52,73} Within this framework, a precipitate undergoes a uniform stress-free transformation strain, ϵ^T , in the absence of a surrounding matrix. The presence of the surrounding matrix then produces a constrained strain, ϵ^C , inside the precipitate. As a result, the precipitate and the matrix both deform and generate an elastic stress field. The elastic strain, ϵ^E , that produces this elastic stress field satisfies

$$\epsilon^C = \epsilon^T + \epsilon^E. \quad (\text{A1})$$

When a precipitate is an inclusion and both the inclusion and the matrix are isotropic, Eshelby has shown that the transformation strain ϵ^T and constrained strain ϵ^C inside the precipitate satisfy

$$\epsilon_{ij}^C = S_{ijkl} \epsilon_{mn}^T, \quad (\text{A2})$$

where S_{ijkl} is referred to as the Eshelby tensor.⁴⁹

Asaro and Barnett⁷⁴ later proved that Eq. (A2) is also valid for an anisotropic spheroidal inclusion embedded in an anisotropic matrix. They showed the Eshelby tensor for an oblate spheroidal inclusion in the cubic symmetric matrix can also be computed by

$$S_{ijmn} = w_{ijkl} c_{klmn}, \quad (\text{A3})$$

$$w_{ijkl} = \frac{abc}{8} \int_0^{2\pi} d\theta \int_0^\pi \frac{\sin \varphi (Z_i Z_l M_{jk}^{-1} + Z_j Z_l M_{ik}^{-1})}{[\sin^2 \varphi (a^2 \cos^2 \theta + b^2 \sin^2 \theta) + c^2 \cos^2 \varphi]^3} d\varphi, \quad (\text{A4})$$

$$\mathbf{Z} = [\sin \varphi \cos \theta, \sin \varphi \sin \theta, \cos \varphi], \quad (\text{A5})$$

$$M_{ik} = c_{ijkl} Z_j Z_l. \quad (\text{A6})$$

Equations (A3)–(A6) may be solved in a Cartesian coordinate system in which the coordinate axis is represented by $[x_1, x_2, x_3]$ and φ is the angle between the unit vector \mathbf{Z} and the axis x_3 . The principal semiaxes of the spheroid (represented by its length) a , b , and c are parallel to the axes x_1 , x_2 , and x_3 , respectively. The c_{ijkl} are the elastic constants of the matrix.

After the Eshelby tensor of an inclusion is evaluated, it may then be used to obtain the analytical expression of the elastic strain energy per unit volume of an anisotropic inhomogeneity in an anisotropic matrix, by using the theory of Lee and Johnson^{49,63} under the general framework of the equivalent inclusion method.^{50–52,73}

REFERENCES

- Tan, E. Gardner, and W. Tice, *Appl. Phys. Lett.* **30**, 175 (1977).
- R. J. Falster and V. V. Voronkov, *Rapid Thermal Processing and the Control of Oxygen Precipitation Behaviour in Silicon Wafers* (Trans Tech Publications, 2008), p. 45.
- K. Sumino and I. Yonenaga, *Semicond. Semimet.* **42**, 449 (1994).
- A. Borghesi, B. Pivac, A. Sassella, and A. Stella, *J. Appl. Phys.* **77**, 4169 (1995).
- N. Inoue, J. Osaka, and K. Wada, *J. Electrochem. Soc.* **129**, 2780 (1982).
- J. Vanhellemont and C. Claeys, *J. Appl. Phys.* **62**, 3960 (1987).
- M. Schrems, *Simulation of Oxygen Precipitation and Denuded Zone Formation during Thermal Anneals* (Trans Tech Publications, 1993), p. 231.
- K. Sueoka, N. Ikeda, T. Yamamoto, and S. Kobayashi, *J. Appl. Phys.* **74**, 5437 (1993).
- J. Vanhellemont, *J. Appl. Phys.* **78**, 4297 (1995).
- J. Esfandyari, C. Schmeiser, S. Senkader, G. Hobler, and B. Murphy, *J. Electrochem. Soc.* **143**, 995 (1996).
- S. Senkader, G. Hobler, and C. Schmeiser, *Appl. Phys. Lett.* **69**, 2202 (1996).
- J. Vanhellemont, *Appl. Phys. Lett.* **68**, 3413 (1996).
- K. F. Kelton, R. Falster, D. Gambaro, M. Olmo, M. Cornara, and P. F. Wei, *J. Appl. Phys.* **85**, 8097 (1999).
- B. G. Ko and K. D. Kwack, *J. Appl. Phys.* **85**, 2100 (1999).
- V. V. Voronkov and R. Falster, *J. Electrochem. Soc.* **149**, G167 (2002).
- Z. Wang, “Modeling microdefects formation in crystalline silicon: The roles of point defects and oxygen,” Ph.D. thesis (Massachusetts Institute of Technology, 2002).
- K. Sueoka, M. Akatsuka, M. Okui, and H. Katahama, *J. Electrochem. Soc.* **150**, G469 (2003).
- J. Vanhellemont, O. De Gryse, and P. Clauws, *Appl. Phys. Lett.* **86**, 221903 (2005).
- J. L. Katz and H. Wiedersich, *J. Chem. Phys.* **55**, 1414 (1971).
- V. Voronkov and R. Falster, *J. Cryst. Growth* **194**, 76 (1998).
- T. A. Frewen, S. S. Kapur, W. Haeckl, W. von Ammon, and T. Sinno, *J. Cryst. Growth* **279**, 258 (2005).
- T. Tan and W. Taylor, *Semicond. Semimet.* **42**, 353 (1994).
- W. Zulehner, G. Harbeke, and M. Schulz, *Springer Series in Material Science* (Springer-Verlag, Berlin, 1989), Vol. 13, p. 127.
- S. A. Campbell, *The Science and Engineering of Microelectronic Fabrication* (Oxford University Press, USA, 1996).
- M. Akatsuka, M. Okui, N. Morimoto, and K. Sueoka, *Jpn. J. Appl. Phys.* **40**, 3055 (2001).
- J. Mikkelsen, *The Diffusivity and Solubility of Oxygen in Silicon* (Cambridge University Press, 1985), p. 19.
- S. Senkader, P. Wilshaw, and R. Falster, *J. Appl. Phys.* **89**, 4803 (2001).
- T. A. Frewen, T. Sinno, W. Haeckl, and W. von Ammon, *Comput. Chem. Eng.* **29**, 713 (2005).

- ²⁹Y. Yang, "Quantitative modeling of oxygen precipitation in silicon," Ph.D. thesis (University of Pennsylvania, 2017).
- ³⁰V. Dragoi, E. Pabo, J. Burggraf, and G. Mittendorfer, *Microsyst. Technol.* **18**, 1065 (2012).
- ³¹T. Plach, V. Dragoi, F. Murauer, and K. Hingerl, *ECS Trans.* **16**, 549 (2008).
- ³²T. Plach, K. Hingerl, S. Tollabimazraehno, G. Hesser, V. Dragoi, and M. Wimplinger, *J. Appl. Phys.* **113**, 094905 (2013).
- ³³K. Schjolberg-Henriksen, S. Moe, M. M. V. Taklo, P. Storås, and J. H. Ulvensoen, *Sens. Actuators A* **142**, 413 (2008).
- ³⁴T. Suni, K. Henttinen, I. Suni, and J. Mäkinen, *J. Electrochem. Soc.* **149**, G348 (2002).
- ³⁵Q. Y. Tong, U. Gösele, and Electrochemical Society, *Semiconductor Wafer Bonding: Science and Technology* (John Wiley, New York, 1999).
- ³⁶W. P. Maszara, G. Goetz, A. Caviglia, and J. B. McKitterick, *J. Appl. Phys.* **64**, 4943 (1988).
- ³⁷Y. Tu and J. Tersoff, *Phys. Rev. Lett.* **84**, 4393 (2000).
- ³⁸F. Wooten, K. Winer, and D. Weaire, *Phys. Rev. Lett.* **54**, 1392 (1985).
- ³⁹G. Hadjisavvas, I. N. Remediakis, and P. C. Kelires, *Phys. Rev. B* **74**, 165419 (2006).
- ⁴⁰L. Kong and L. J. Lewis, *Phys. Rev. B* **77**, 165422 (2008).
- ⁴¹P. Kroll and H. J. Schulte, *Phys. Status Solidi (b)* **243**, R47 (2006).
- ⁴²F. Djurabekova and K. Nordlund, *Phys. Rev. B* **77**, 115325 (2008).
- ⁴³C. Y. Chuang, Q. M. Li, D. Leonhardt, S. M. Han, and T. Sinno, *Surf. Sci.* **609**, 221 (2013).
- ⁴⁴P. F. Wei, K. F. Kelton, and R. Falster, *J. Appl. Phys.* **88**, 5062 (2000).
- ⁴⁵B. C. Trzynadlowski and S. T. Dunham, *J. Appl. Phys.* **114**, 243508 (2013).
- ⁴⁶S. Senkader, J. Esfandyari, and G. Hobler, *J. Appl. Phys.* **78**, 6469 (1995).
- ⁴⁷T. A. Frewen, "A modular framework for predictive modeling of microstructural evolution in silicon materials processing," Ph.D. thesis (University of Pennsylvania, 2004).
- ⁴⁸T. Sinno and R. A. Brown, *J. Electrochem. Soc.* **146**, 2300 (1999).
- ⁴⁹J. K. Lee and W. C. Johnson, *Acta Metall.* **26**, 541 (1978).
- ⁵⁰J. Eshelby, *The Elastic Field Outside an Ellipsoidal Inclusion* (The Royal Society, 1959), p. 561.
- ⁵¹J. D. Eshelby, *The Determination of the Elastic Field of an Ellipsoidal Inclusion, and Related Problems* (The Royal Society, 1957), p. 376.
- ⁵²J. D. Eshelby, *Elastic Inclusions and Inhomogeneities* (North-Holland Publishing Company, Amsterdam, 1961), Vol. 2.
- ⁵³G. Kissinger, D. Kot, J. Dabrowski, V. Akhmetov, A. Sattler, and W. Von Ammon, *ECS Trans.* **16**, 97 (2008).
- ⁵⁴K. Yasutake, M. Umeno, and H. Kawabe, *Phys. Status Solidi (a)* **83**, 207 (1984).
- ⁵⁵M. Hopcroft, W. D. Nix, and T. W. Kenny, *J. Microelectromech. Syst.* **19**, 229 (2010).
- ⁵⁶G. Kissinger, T. Müller, A. Sattler, W. Häckl, P. Krottenthaler, T. Grabolla, H. Richter, and W. von Ammon, *Mater. Sci. Semicond. Process.* **9**, 236 (2006).
- ⁵⁷J. Nicolai, N. Burle, C. Serafino, and B. Pichaud, *J. Cryst. Growth* **372**, 138 (2013).
- ⁵⁸E. Dornberger, "Université catholique de Louvain," Thesis, 1997.
- ⁵⁹A. Michel, see <https://github.com/adrianmichel/differential-evolution> for C++ Differential Evolution (2017).
- ⁶⁰F. Biscani and D. Izzo, see <https://github.com/esa/pagmo> for Parallel Global Multiobjective Optimizer (2014).
- ⁶¹D. Izzo, M. Rucinski, and C. Ampatzis, *Parallel Global Optimisation Meta-Heuristics Using an Asynchronous Island-Model* (IEEE, 2009), p. 2301.
- ⁶²D. Izzo, M. Ruciński, and F. Biscani, *Parallel Architectures and Bioinspired Algorithms* (Springer, 2012), p. 151.
- ⁶³M. Ruciński, D. Izzo, and F. Biscani, *Parallel Comput.* **36**, 555 (2010).
- ⁶⁴O. Tange, *GNU Parallel 2018* (Lulu.com, 2018).
- ⁶⁵G. Kissinger, J. Dabrowski, T. Sinno, Y. Yang, D. Kot, and A. Sattler, *J. Cryst. Growth* **468**, 424 (2016).
- ⁶⁶R. C. Tolman, *J. Chem. Phys.* **17**, 333 (1949).
- ⁶⁷M. N. Joswiak, N. Duff, M. F. Doherty, and B. Peters, *J. Phys. Chem. Lett.* **4**, 4267 (2013).
- ⁶⁸L. Wu, Q. Li, B. Xu, and W. Liu, *J. Mater. Res.* **31**, 3649 (2016).
- ⁶⁹G. Kissinger and J. Dabrowski, *J. Electrochem. Soc.* **155**, H448 (2008).
- ⁷⁰K. S. Brown, C. C. Hill, G. A. Calero, C. R. Myers, K. H. Lee, J. P. Sethna, and R. A. Cerione, *Phys. Biol.* **1**, 184 (2004).
- ⁷¹K. S. Brown and J. P. Sethna, *Phys. Rev. E* **68**, 021904 (2003).
- ⁷²J. K. Lee, D. Barnett, and H. Aaronson, *Metall. Trans. A* **8**, 963 (1977).
- ⁷³T. Mura, *Micromechanics of Defects in Solids* (Springer Science & Business Media, 2012), Vol. 3.
- ⁷⁴R. J. Asaro and D. M. Barnett, *J. Mech. Phys. Solids* **23**, 77 (1975).